Sensors and Materials, Vol. 37, No. 5 (2025) 2037–2047
MYU Tokyo

S & M 4040

Induction Motor Fault Diagnosis Based on Discrete Fractional Fourier Transform of Stator Current

Feng-Chang Gu,[1] Hung-Cheng Chen,[1*] Jian-Yong Bian,[2]
Chun-Liang Hsu,[2] and Ting-Jui Yang[1]

[1]Department of Electrical Engineering, National Chin-Yi University of Technology,
No. 57, Sec. 2, Zhongshan Rd., Taiping Dist., Taichung 411030, Taiwan (R.O.C.)
[2]Department of Electronic Engineering, Dongguan Polytechnic, Dongguan, Guangdong, China

(Received November 11, 2024; accepted April 23, 2025)

Keywords: discrete fractional Fourier transform, extension, fractal, feature extraction, fault diagnosis

A signal change in stator current often indicates that a variable-frequency motor is malfunctioning. In this study, we developed a method based on discrete fractional Fourier transform (DFrFT) to identify rotor defects in a three-phase induction motor. The first step was to measure the stator current in an induction motor, followed by the application of DFrFT to detect rotor faults. DFrFT is frequently used to transform a time-domain signal at different angles. Angles from 0–2π were divided into 20 equal sections, which were sequentially transformed to construct characteristic matrices. For clearer characteristic information, the fractal method was applied to extract features, fractal dimension, lacunarity, and the mean value from the pattern matrices. Finally, defect patterns were identified by applying extension theory. To verify whether the proposed method was feasible for rotor fault recognition in the presence of interference, ±5 to ±15% Gaussian white random noise was added to the current signal. The results indicated that the proposed method can diagnose various rotor defects in a motor.

1. Introduction

Motors are important in industry and our everyday lives. In particular, variable-frequency motors have been widely used in electrical equipment as part of the wider push to decarbonize. These motors conserve energy, require low maintenance, are highly efficient, and are highly amenable to automation. However, motor performance is difficult to maintain. Degradation and malfunctions in motors can be commercially expensive.(1,2) Therefore, the long-term monitoring and diagnosis of motors are necessary.

The Electric Power Research Institute reported that 53% of all motor problems originate from mechanical faults, such as bearing faults, unbalanced motors, or loose components.(3) This implies that 47% of all motor problems occur owing to electrical faults, of which 37% are attributed to stator winding faults and the remaining 10% are attributed to rotor faults, such as an unbalanced air gap or a broken rotor bar.(4) In this study, we developed three defect fault

*Corresponding author: e-mail: hcchen@ncut.edu.tw
https://doi.org/10.18494/SAM5471

models based on three commonly occurring faults in induction motors, namely, ball bearing damage, one hollow rotor bar, and three broken rotor bars. A variable-frequency drive (VFD) was used in the test to regulate the output frequency at 60 and 50 Hz to ensure that the three defect fault models can be applied to different rotational speeds. The current in the defective stator was measured using an ammeter. The differences between characteristic signals were analyzed using discrete fractional Fourier transform (DFrFT).

Fractal theory has been successful in describing complex shapes, such as coastlines and mountain ranges, where conventional methods have failed.(5,6) A three-dimensional (3D) pattern (β–n–F) image is also a complex shape that can be transformed using DFrFT. Previous studies have successfully employed fractal theory to extract fractal features from 3D (n–q–φ) patterns.(7–9) We also applied fractal theory for 3D pattern (β–n–F) feature extraction. The mean value was added to produce a third characteristic, which was used to determine feature distributions. Finally, the proposed method was evaluated in experiments.

2. Rotor Defect Models and Experimental Platform Architecture

2.1 Defect models

Induction motors degrade when operated under challenging conditions over prolonged periods.(10–12) In this study, we defined four types of squirrel cage induction motor: a Type A motor had three broken rotor bars, a Type B motor had one hollow rotor bar, a Type C motor had ball bearing damage, and a Type D motor was a normal induction motor (Fig. 1). These models were used

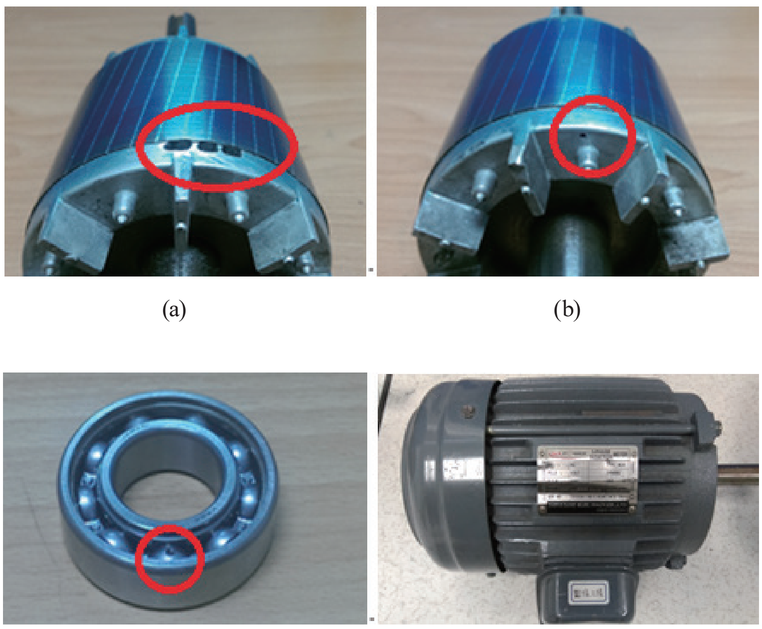

(a) (b) (c) (d)

Fig. 1. (Color online) Types of defect in an induction motor rotor. (a) Type A, (b) type B, (c) type C, and (d) type D.

to identify rotor defects and analyze their characteristics. The CNS-C-4088 series of induction motors (Cherng Chang Elec. Mach, Taipei, Taiwan) was used; it has a rated output of 1.5 kW and speeds of 1750 rpm at 60 Hz and 1450 rpm at 50 Hz. The rated power for the delta connection was 220 V, and that for the Y connection was 380 V.

2.2 Experimental platform

The experimental platform is shown in Fig. 2. The first device is a powder brake, which is used to simulate magnetic loads of differing intensities. The second device is the 1.5 kW three-phase 4P squirrel cage induction motor. The third device is an SS2 series VFD (Shihlin Electric, Taiwan) that is rated for the three-phase power voltage of 200–240 V at 50 or 60 Hz.

The motor was operated at the rated rotational speed, with the powder brake providing the motor load. The motor speed was regulated by the VFD. The rated rotational speeds were 1750 rpm at 60 Hz and 1450 rpm at 50 Hz. The stator current in the experimental model was measured using an ammeter. Finally, an analysis program was used for the initial signal processing. It included notch filters to filter power base frequency and low-pass filters to filter high-frequency noise. A spectrum analysis was performed using the fractional Fourier transform (FrFT).[13] The structure of the experimental platform is shown in Fig. 3.

3. FrFT

3.1 Theory introduction

The FrFT of the original signal $x(t)$ with an angle α, denoted by $F^{\beta}[x](u)$, is defined as[14]

$$F^{\beta}[x](u) = \int_{-\infty}^{+\infty} x(t) K_{\alpha}(u,t) dt, \tag{1}$$

where α is the rotation angle defined as $\beta(\pi/2)$, β is the order of the FrFT, and u corresponds to the time point when $\alpha = 0$ and to the frequency when $\alpha = \pi/2$. The transform kernel $K_{\alpha}(u,t)$ is defined as

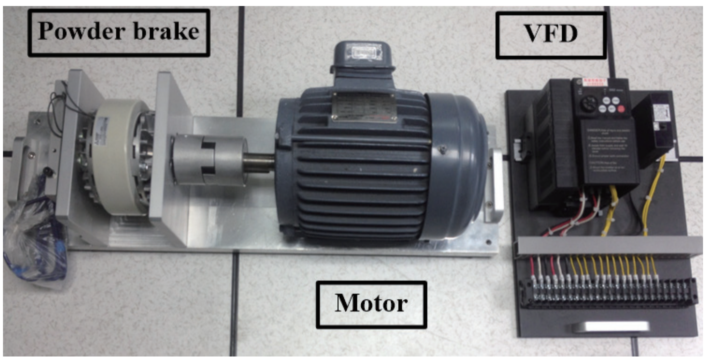

Fig. 2. (Color online) Experimental platform.

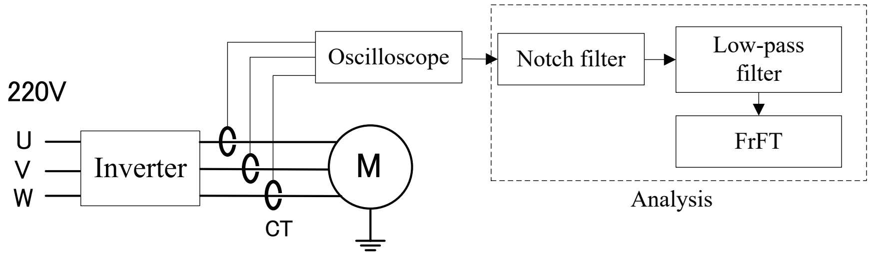

Fig. 3. Structure of experimental platform.

$$K_\alpha(u,t)=\begin{cases}\sqrt{\dfrac{1-j\cot(\alpha)}{2\pi}}e^{j\frac{(t^2+u^2)}{2}\cot(\alpha)-jut\csc(\alpha)}, & \alpha\neq n\pi\\ \delta(t-u), & \alpha=2n\pi\\ \delta(t+u), & \alpha=2n\pi\pm\pi\end{cases}\tag{2}$$

where $n\in Z$. For the order of β, the kernel $K_\alpha(u,t)$ was a chirp signal with a linear frequency and a rate of $\cot(\alpha)$, the initial frequency of $u\csc(\alpha)$. An envelope can be defined as

$$\sqrt{(1-j\cot(\alpha)/2\pi}\exp(ju^2/2\cot(\alpha)).\tag{3}$$

The FrFT $F^\beta[x](u)$ was interpreted as a rotation by the angle α in the time–frequency plane. $F^{\pi/2}$ corresponded to the classical Fourier transform. The angle when the FrFT was run continually was a simple sum equal to the angle of continuous rotation. The signal was also explained as the chirp decomposition of the signal. This physical interpretation of the FrFT was used to detect chirp-like signals, such as the signal generated by fault harmonics when discharges occur.(15) The DFrFT was defined as

$$\tilde{F}^\beta[x](u)=\sqrt{\frac{1-j\cot(\alpha)}{2\pi}}T_s e^{j\left(\frac{u^2}{2}\right)\cot(\alpha)}\cdot\sum_{-\infty}^{+\infty}e^{j\left(\frac{n^2T_s^2}{2}\right)\cot(\alpha)-jnT_s u\csc(\alpha)}x[n],\tag{4}$$

where T_s denotes the sampling period. The DFrFT can be implemented through several methods, which differ in their computational complexity and accuracy. The eigen-decomposition method was used in this study.(16) The N-point DFrFT was defined by its transformation matrix and described as

$$F^\beta[m,n]=\sum_{k=0}^{N-1}u_k[m]e^{-j\frac{\pi}{2}k\beta}u_k[n],\tag{5}$$

where $u_k[n]$ represents a discrete Hermite–Gaussian function. The DFrFT has the advantage of having a low computational complexity $O(N \log N)$. The discrete signal $x[n]$ is obtained as

$$F^{\beta} x[n] = \sum_{k=0}^{N-1} u_k[m] e^{-j\frac{\pi}{2}k\beta} u_k[n] \cdot x[n]. \tag{6}$$

3.2 3D characteristic spectrum

A 3D characteristic spectrum was constructed using the DFrFT of the current signal in the range of [0, π/2]. This is an effective means to reveal the change in energy distribution from the time domain to the frequency domain. The 3D pattern was then subjected to feature extraction to identify the type of defect. In this paper, we propose the concept of amplitude conversion ratio to compare the amplitude conversion rates of different types of current signal. $\eta(n)$ denotes the absolute value of the quotient of $F^{\beta}x[n]$, the DFrFT of $x[n]$, which was defined as

$$\eta(n) = \left| \frac{F^{\beta} x[n]}{x[n]} \right|. \tag{7}$$

Fractal features were subsequently extracted using 3D β–n–η patterns to identify the different experimental types.(7) The first step of the feature extraction was determining the increment of α ($\Delta\alpha$) using the value of $\Delta\beta$. To reduce the computational load of the DFrFT, 20 transformations were performed with α in [0, π/2] and $\Delta\alpha = 4.5°$ ($\Delta\beta = 0.05$). First, the discrete Hermite–Gaussian function $u_a[n]$ and the matrix $F^{\beta}[m,n]$ were calculated, which was multiplied by the original discharge signal $x[n]$ to obtain $F^{\beta}x[n]$, as illustrated in Eq. (6). Eventually, a 3D characteristic pattern was created through 20 successive transforms, after the amplitude transform ratio η was determined using Eq. (7).

4. Experiment Results and Discussion

Stator currents in the different experimental models were measured and analyzed. The data for each model were obtained every 10 s, and the sampling rate was 100 kS/s. Different numbers of data points were acquired for each frequency. After the data were pretreated as described in Sect. 2, two power cycle current signals were captured for analysis. Figures 4 and 5 show the trends in stator current after signal pretreatment when the experimental model was operated at 60 and 50 Hz, respectively. However, the use of these signals alone is insufficient for determining how well the rotor defect models perform against each other. Therefore, these signals were transformed into a 3D pattern (β–n–F) by the DFrFT. In this study, 30 sets of measurements were taken for each experimental model; 15 sets were randomly selected to determine the extension classical domain, and the remaining 15 sets were used for evaluating the test pattern.

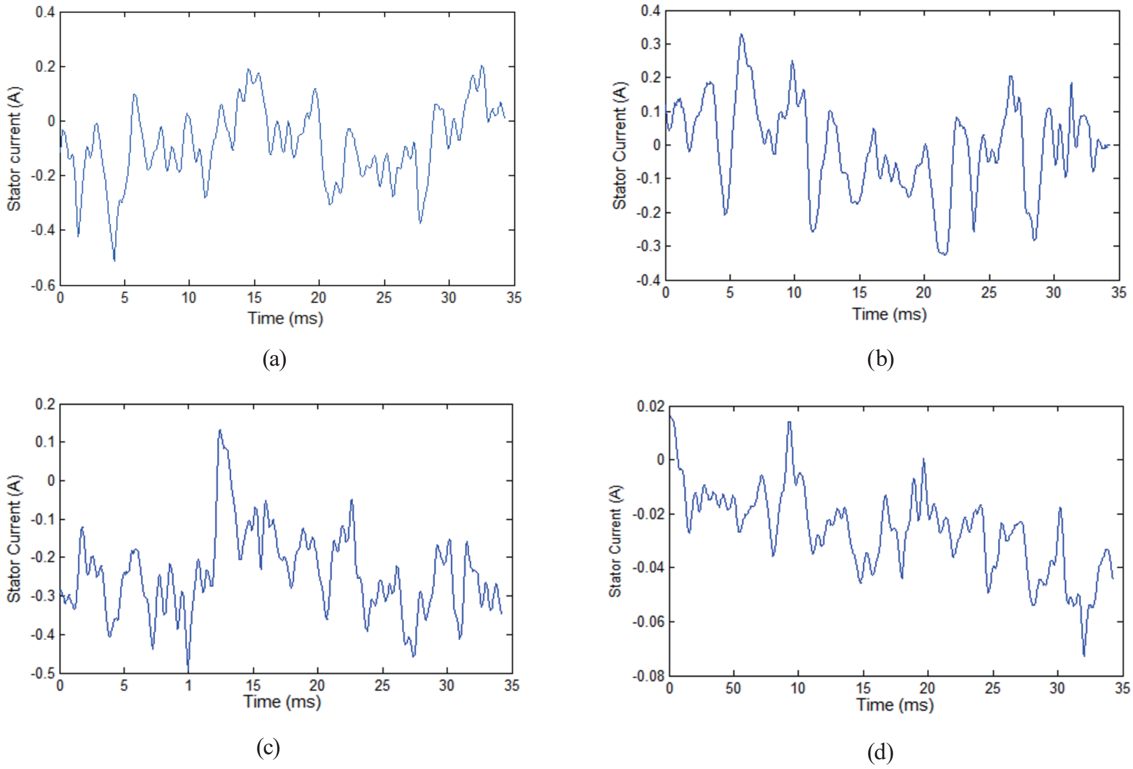

Fig. 4. (Color online) Stator current when the model was operated at 60 Hz. (a) Type A, (b) Type B, (c) Type C, and (d) Type D.

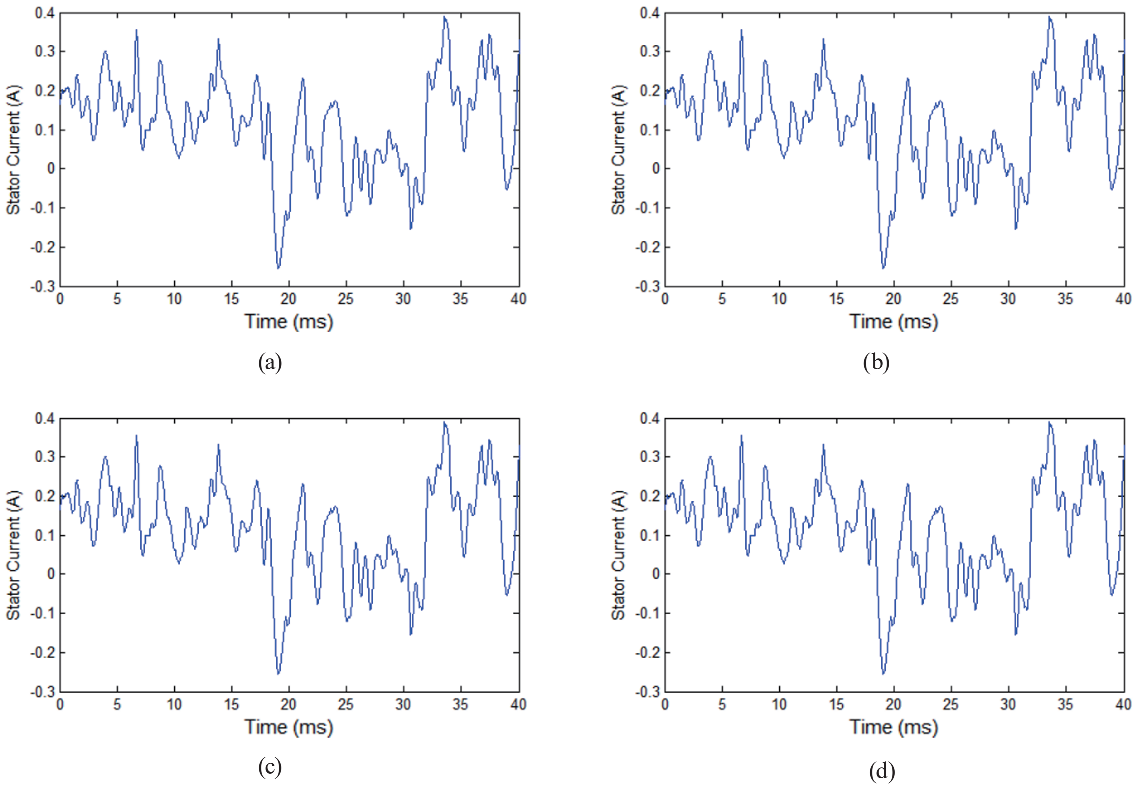

Fig. 5. (Color online) Stator current when the model was operated at 50 Hz.(a) Type A, (b) Type B, (c) Type C, and (d) Type D.

4.1 3D (β–n–F) pattern

The stator current was continuously converted from the time domain to the frequency domain to establish a characteristic pattern. The β–n–F characteristic 3D patterns of the stator current signal at 60 and 50 Hz are shown in Figs. 6 and 7, respectively. These figures suggest that each type of current had a different β–n–F 3D characteristic pattern. However, identifying experimental patterns using these maps was difficult. Therefore, fractal characteristic features, fractal dimension, and lacunarity were extracted from the β–n–F 3D pattern of each experimental model.

4.2 Feature extraction

The feature distribution obtained by the proposed method is shown in Fig. 8. Fractal dimension and lacunarity were extracted from all 3D (β–n–F) patterns. The fractal dimensions had a wide distribution for all four experimental models, implying that distinguishing one fault mode from the other was challenging when using fractal dimension alone [Fig. 8(a)]. However,

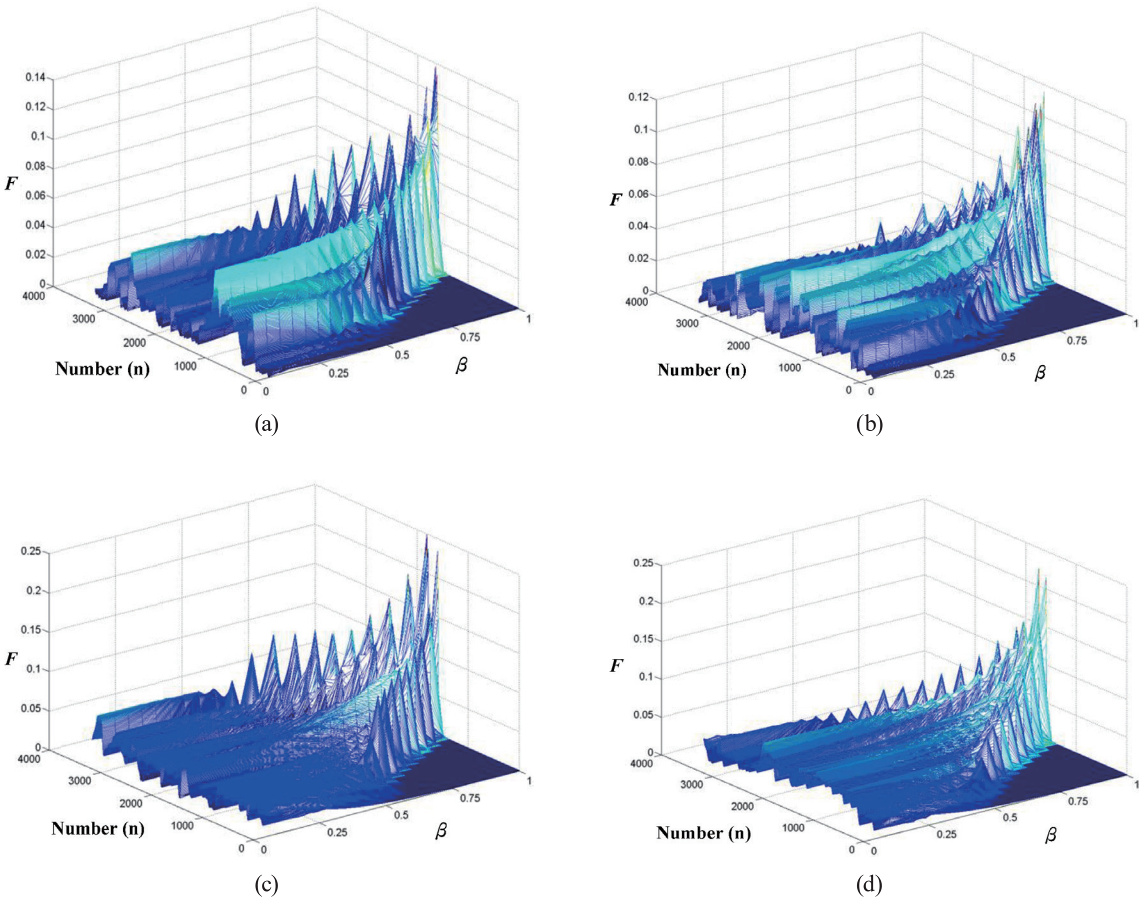

Fig. 6. (Color online) 3D (β–n–F) patterns at 60 Hz. (a) Type A, (b) type B, (c) type C, and (d) type D.

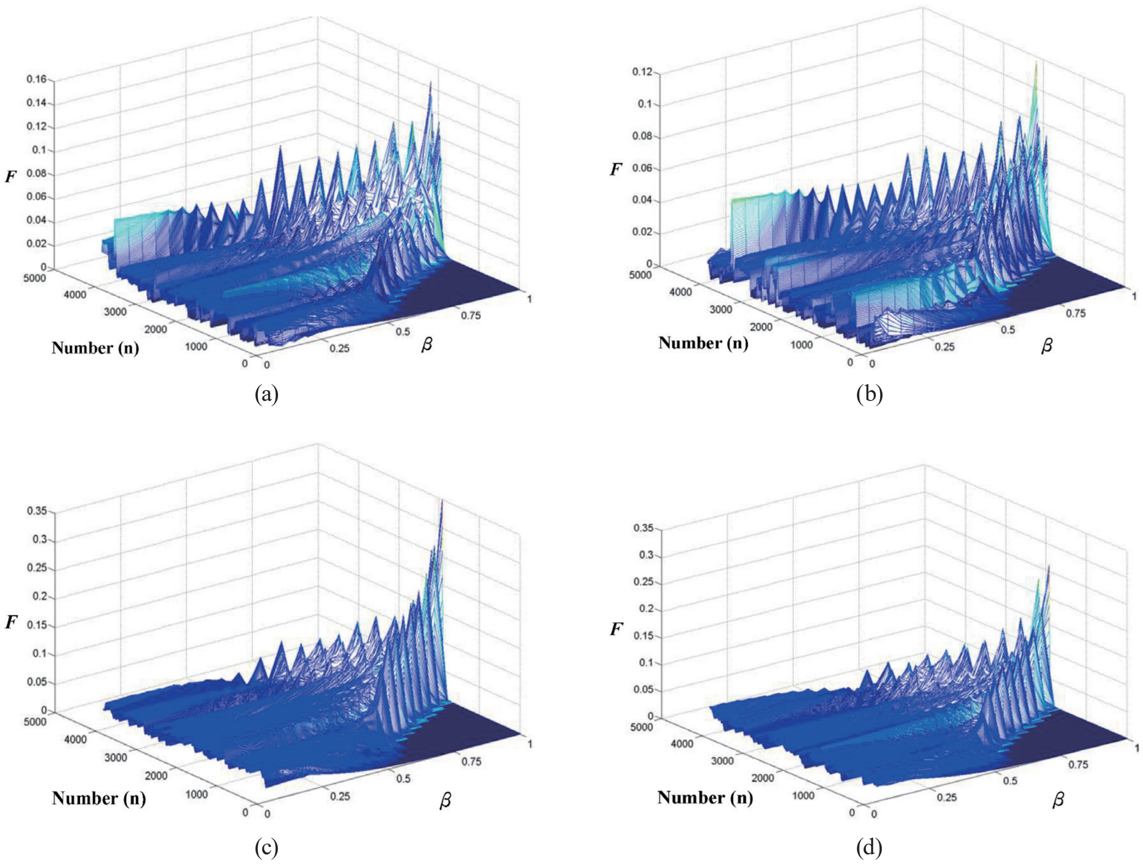

Fig. 7. (Color online) 3D (β–n–F) patterns at 50 Hz. (a) Type A, (b) type B, (c) type C, and (d) type D.

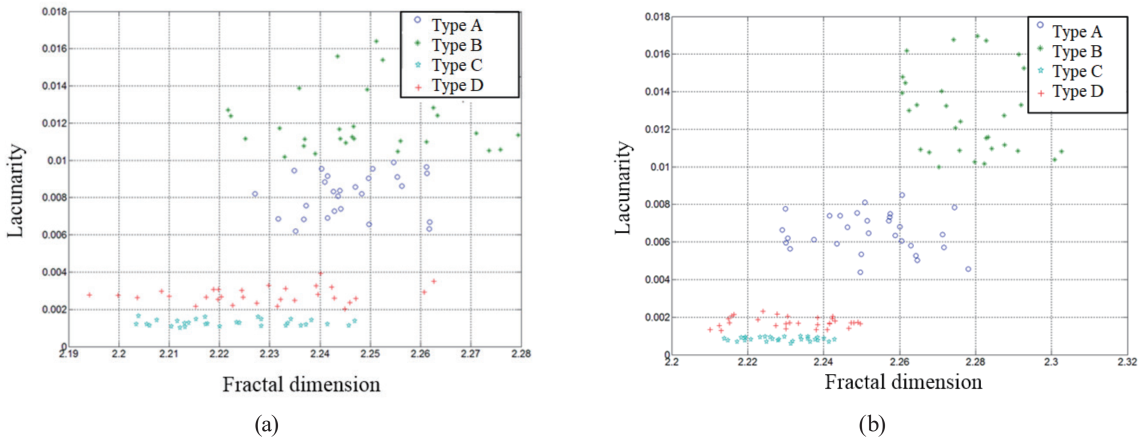

Fig. 8. (Color online) Distribution of fractal features. (a) Motor operating at 60 Hz. (b) Motor operating at 50 Hz.

different experimental models could be distinguished from each other when lacunarity was added to the analysis. For both motor operating frequencies of 50 and 60 Hz, the patterns of any particular experimental model were close to each other. In this study, the mean value extracted from the 3D (β–n–F) pattern was added as the third feature to ensure that the pattern difference was clearer. The fractal feature distribution with the mean value added is shown in Fig. 9. The

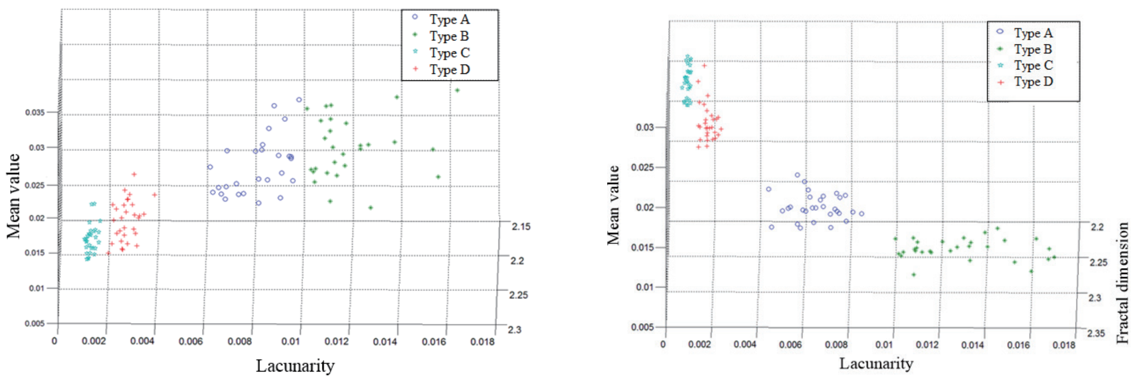

(a) (b)

Fig. 9. (Color online) Distribution of fractal features with a mean value. (a) Motor operating at 60 Hz. (b) Motor operating at 50 Hz

addition of the third feature simplified the task of separating the patterns of each experimental model, compared with the patterns presented in Fig. 8.

4.3 Pattern recognition

In this study, we employed extension theory to extract patterns in rotor defect models because the method of extension recognition involves the concepts of matter elements and extension sets. This method is suitable for solving contradiction problems.(17) The fuzzy membership function has an output within [0, 1]. This interval is extended in an extension set to [−∞, ∞]. Thus, this set can be used to define another set that might include any data point in the domain. Matter elements can easily express the essence of matter, and the extension set is a quantitative tool originating from extension theory. Sets represent the degree of correlation between matter elements on the basis of a correlation function.

The procedure of the extension method has been detailed in previous reports.(18,19) The input for a recognition system may contain noise originating from the detector or the environment. To verify the feasibility of the proposed method for recognizing stator current signal patterns, random Gaussian white noise was simulated and added to the measured stator current signals. The following four cases of pattern recognition results were obtained:
Case 1: Pattern recognition using fractal features at 60 Hz [Fig. 8(a)].
Case 2: Pattern recognition using fractal features at 50 Hz [Fig. 8(b)].
Case 3: Pattern recognition using fractal features with a mean value at 60 Hz [Fig. 9(a)].
Case 4: Pattern recognition using fractal features with a mean value at 50 Hz [Fig. 9(b)].

Tables 1 and 2 present the accuracy rates of pattern recognition based on fractal features. The recognition rate was 100% in the absence of extra noise. The average recognition rate decreased as the amount of random white noise increased. When the amount of random white noise increased by 15%, the average recognition rate decreased from 81.7% to 78.3%. To improve the recognition rate, a third feature was added to the mean value in this study. The subsequent recognition results are listed in Tables 3 and 4. The average recognition rate increased for all

Table 1
Recognition accuracy rates (%) when using fractal features at 60 Hz.

Model	Noise			
	0%	±5%	±10%	±15%
Type A	100	93.3	86.7	73.3
Type B	100	93.3	80	80
Type C	100	93.3	86.7	80
Type D	100	100	100	93.3
Average	100	95	88	81.7

Table 2
Recognition accuracy rates (%) when using fractal features at 50 Hz.

Model	Noise			
	0%	±5%	±10%	±15%
Type A	100	100	86.7	80
Type B	100	93.3	86.7	80
Type C	100	93.3	80	73.3
Type D	100	93.3	93.3	80
Average	100	95	86.7	78.3

Table 3
Recognition accuracy rates (%) when using fractal features with mean discharge at 60 Hz.

Model	Noise			
	0%	±5%	±10%	±15%
Type A	100	100	93.3	86.7
Type B	100	100	93.3	86.7
Type C	100	93.3	93.3	80
Type D	100	100	93.3	86.7
Average	100	98.3	93.3	85

Table 4
Recognition accuracy rates (%) when using fractal features with mean discharge at 50 Hz.

Model	Noise			
	0%	±5%	±10%	±15%
Type A	100	100	93.3	86.7
Type B	100	100	86.7	86.7
Type C	100	93.3	86.7	80
Type D	100	93.3	93.3	80
Average	100	96.6	90	83.3

cases after the addition of the third feature. When 15% of random white noise was added, the average recognition rate decreased from 85 to 83.3%.

5. Conclusion

We presented a motor current signature analysis tool based on the DFrFT as an effective pattern recognition method for identifying rotor defects in induction motors. The DFrFT described the gradual transition characteristics from the frequency domain to the time domain as the transform order was increased from zero to unity, followed by the construction of a 3D (β–n–F) matrix. Furthermore, fractal theory was introduced to extract the fractal dimension, lacunarity, and mean value. Finally, extension theory was applied to achieve the pattern recognition of motor defects. The performance of the proposed method in the presence of interference was assessed by adding ±5 to ±15% of random Gaussian noise to the current signal. The results suggest that the pattern recognition method can distinctly discriminate between different types of motor defect, even at different frequencies. These results verify the effectiveness of the proposed method in detecting motor failures, aiding quality control.

Acknowledgments

The research was supported by the National Science and Technology Council of the Republic of China under Grant No. NSTC 112-2221-E-167 -018.

References

1 R. Zhang, K. C. Wang, L. Wu, and H. Gao: Sens. Mater. **34** (2022) 765. https://doi.org/10.18494/SAM3636
2 V. Fernandez-Cavero, D. Morinigo-Sotelo, O. Duque-Perez, and J. Pons-Llinares: IEEE ACCESS **5** (2018) 8048. https://doi.org/10.1109/ACCESS.2017.2702643
3 J. Stein: EPRI Technical Report (2003). https://www.epri.com/research/products/000000000001008377
4 S. Choi, E. Pazouki, J. Baek, and H. R. Bahrami: IEEE Trans. Ind. Electron. **62** (2015) 1760. https://doi.org/10.1109/TIE.2014.2361112
5 B. B. Mandelbrot: New York: Freeman (1983).
6 L. L. Zhang, T. C. Chang, and Y. M. Mao: Sens. Mater. **32** (2020) 2017. https://doi.org/10.18494/SAM.2020.2792
7 L. Satish and W. S. Zaengl: IEEE Trans. Dielectr. Electr. Insul. **2** (1995) 352. https://doi.org/10.1109/94.395421
8 F. C. Gu, H. C. Chang, and C. C. Kuo: IEEE Trans. Dielectr. Electr. Insul. **20** (2013) 1049. https://doi.org/10.1109/TDEI.2013.6571416
9 Y. Wang, Z. Wang, and J. Li: IEEE Antennas Wirel. Propag. Lett. **16** (2017) 852. https://doi.org/10.1109/LAWP.2016.2609916
10 G. Didier, E. Ternisien, O. Caspary, and H. Razik: IEEE Trans. Ind. Appl. **42** (2006) 79. https://doi.org/10.1109/TIA.2005.861368
11 M. F. Cabanas, F. Pedrayes, M. G. Melero, C. H. R. García, J. M. Cano, G. A. Orcajo, and J. G. Norniella: IEEE Trans. Instrum. Meas. **60** (2011) 891. https://doi.org/10.1109/TIM.2010.2062711
12 Po. H. Chou, Y. L. Hsu, S. C. Yang, H. C. Chang, Y. C. Kuo, L. F. Chiu, and Y. T. Chen: Sens. Mater. **30** (2018) 2401. https://doi.org/10.18494/SAM.2018.1976
13 S. C. Pei, M. H. Yeh, and C. C. Tseng: IEEE Trans. Signal Process. **47** (1999) 1335. https://doi.org/10.1109/78.757221
14 S. C. Pei and W. L. Hsue: IEEE Signal Process. Lett. **13** (2006) 329. https://doi.org/10.1109/LSP.2006.871721
15 S. C. Pei, C. C. Tseng, M. H. Yeh, and J. J. Shyu: IEEE Trans. Circuits Syst. II, Analog Digit. Signal Process. **45** (1998) 665. https://doi.org/10.1109/82.686685
16 D. Y. Wei, Q. W. Ran, Y. M. Li, J. Ma, and L.Y. Tan: IET Signal Process. **5** (2011) 150. https://doi.org/10.1049/iet-spr.2009.0288
17 M. H. Wang and C. Y. Ho: IEEE Trans. Power Del. **20** (2005) 1939. https://doi.org/10.1109/TPWRD.2005.848673
18 F. C. Gu, H. C. Chen, and M. H. Chao: Appl. Sci. **7** (2017) 1021. https://doi.org/10.3390/app7101021
19 F. C. Gu, H. C. Chang, F. H. Chen, and C. C. Kuo: Expert Syst. **39** (2012) 2804. https://doi.org/10.1016/j.eswa.2011.08.140